# 3D Printing Fabrication of Amorphous Thermoelectric Materials with Ultralow Thermal Conductivity

*Minhong He, Yan Zhao, Biao Wang, Qing Xi, Jun Zhou,\* and Ziqi Liang\**

The 3D printing technology, which was first reported by Hull,[1] has been rapidly developing in recent years with the advances of precision measuring and control technology. One 3D printing method is based on the photoresins, which is realized primarily through three routes of sterolithography apparatus (SLA), digital light processing (DLP), and 3D spray printing (3DSP).[2] The principle of this technology relates to building up the objects by optically curing liquid photoresins during the layer-by-layer printing processes.[3,4] The 3D printing of photoresins, which exhibits the advantages of cost-effective utilization, high building accuracy, and fast fabrication, has been widely applied to rapid prototyping and manufacturing.[5–7] In the past several years, there has been considerable interest in the application of 3D printing technologies for creating bionic ear,[8] "reactionware" for chemical science,[9,10] flow plates for water electrolysis,[11] lithium-ion microbattery,[12] bone scaffolds,[13] multifunctional microsystems,[14] cell-laden tissue constructs,[15] lightweight cellular composites,[16] and so on.

Of unique advantages, 3D printing enables the generation of free-standing bulk objects, which are particularly useful for preparing thermoelectric (TE) material samples. Unfortunately, there has no report yet on this utility. By contrast, traditional methods of making TE samples involve hot-pressing,[17,18] melt spinning, and spark plasma sintering,[19] all of which rendered enormous challenges for cost-effective, high-throughput production of TE modules.

Herein we report for the first time a 3D fabrication of amorphous TE materials, which represents a new manufacturing paradigm other than conventional hot-pressing

methods. We show that the 3D printing fabrication method offers a facile and promising way to obtain "electron-crystal phonon-glass" TE materials.[20–22] In this work, we chose the classical TE materials—p-type $Bi_{0.5}Sb_{1.5}Te_3$ (BST) alloys which are the best commercial TE materials at room temperature—as a proof-of-concept. BST samples are obtained by 3D fabrication followed by thermal annealing. Amorphous characteristics with ultralow thermal conductivity,[23–25] which are favorable for TE applications, are found.

**Figure 1** depicts the schematic steps of 3D printing and 3D fabrication of BST samples, respectively, followed by thermal annealing process, which removes the template of photoresins while forming crystalline BST nanoparticles. Composite resins used in these 3D processes are a mixture of BST powders and photoresins at various loading ratios of BST. BST powders were prepared by mixing Bi, Sb, and Te granules, followed by ball milling for 100 h. Photoresins used for 3D printing and 3D fabrication are Formlabs Clear Photoresins (chemical structures are not disclosed) and our customized photoresins, respectively. Our photoresin formulations comprise epoxy resin of 3,4-epoxycyclohexylmethyl-3,4-epoxycyclohexane carboxylate, diluent of 3-ethyl-3-oxetanemethanol, cationic photoinitiator of triarylsulfonium hexafluoroantimonate salts, and photosensitizer of PSS-303 (Scheme S1, Supporting Information).

In general, 3D printed photoresins serve as versatile templates, allowing one to generate any complicated shapes of BST samples at a much lower cost than those by hot-pressing moulds. As shown in route (a) in Figure 1, the printing was performed on a Form1+ SLA 3D printer at a layer-height of 100 μm. The computer aided design (CAD) model stereo lithography (STL) files were first input into the Formlabs' custom-built PreForm software. Then the printing job started after pouring the composite resins into the tank. The detailed printing process is shown in Movie S1 (Supporting Information). Upon the completion of printing, excess resins were washed away from the BST samples by using isopropanol (IPA). Finally, the samples were thermally annealed under atmospheric pressure in a tubular furnace at 350 °C to remove the photoresins, producing the BST materials. Nevertheless, a challenge was encountered during the above processes. When the BST contents were more than 5 wt%, the samples could not be printed successfully because we are currently not authorized to adjust the printing speed of Form1+ SLA 3D printer whose custom-built PreForm software is not open-source yet. Such a low BST content (≤5 wt%) is unfortunately useless for TE applications. Once we are authorized

M. He, Y. Zhao, Prof. Z. Liang
Department of Materials Science
Fudan University
Shanghai 200433, China
E-mail: zqliang@fudan.edu.cn

B. Wang, Q. Xi, Prof. J. Zhou
Center for Phononics and Thermal Energy Science
School of Physics Science and Engineering
Tongji University
Shanghai 200092, China
E-mail: zhoujunzhou@tongji.edu.cn

Y. Zhao
Shanghai Advanced Research Institute
Chinese Academy of Sciences
Shanghai 201210, China
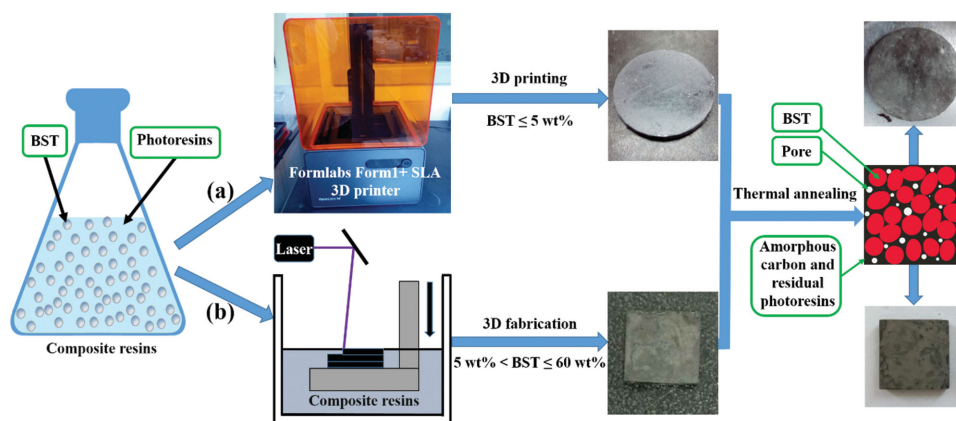
**Figure 1.** Schematic routes of a) 3D printing and b) 3D fabrication of BST samples mixed with Formlabs Clear Photoresins and our customized phtoresins, respectively, followed by thermal annealing.

to tune the printing speed, high-contents of BST samples can be printed.

As an alternative solution, we mimicked the 3D printing principle and photocured the resins by optical equipment in a layer-by-layer fashion to fabricate BST samples with the contents of 40, 50, and 60 wt%, respectively. Such 3D fabrication, in analogy to 3D printing, is schematically shown in route (b) in Figure 1. In our early attempts, the composite resins containing Formlabs Clear Photoresins and high contents of BST powders failed to be photocured. Thus, we formulated our photoresins (see the Supporting Information for details of resin formulation procedures), which enables to photocure successfully the composite resins with high contents of BST nanoparticles. Likewise, a thermal annealing step was conducted in the final stage to remove the template of photoresins.

In order to determine the optimal temperature of thermal annealing, we studied thermal behavior of 3D fabricated samples by using thermogravimetric analysis (TGA) measurement. Figure S1 (Supporting Information) compares the weight loss profiles of composite resins with 60 wt% BST powders, taken as an example, and our customized photoresins. Customized photoresin samples exhibit a two-step process of weight loss in the range of 30–600 °C. The first step is attributed to the loss of volatile solvent while the second is due to the decomposition of macromolecular chains and the oxidation of char residues. Furthermore, derivative thermo-gravimetric analysis (DTG) profiles (Figure S1, Supporting Information) were obtained from TGA results, showing the mass loss rate. There exist two DTG peaks at 350 and 425 °C for composite resin samples, in contrast to 325 and 437 °C for pure photoresin samples. We initially chose 425 °C for thermal annealing of 3D fabricated BST samples, which however caused lots of cracking in the samples. Then we used 350 °C with various thermal annealing times, which gave high-quality samples for the following measurements.

We then investigated the influence of thermal annealing process on 3D fabricated composite resin samples by studying their crystalline structures and bulk morphology by X-ray diffraction (XRD) measurement and field-effect scanning electron microscopy (FE-SEM), respectively. **Figure 2**a shows the XRD patterns of 3D fabricated 60 wt% BST samples with different thermal annealing time. It can be seen that the unannealed sample is in two phases which consist of Te and a solid solution of Bi and Sb, while thermally annealed samples show a single-phase of BST. All patterns are in good agreement with the standard JCPDS XRD pattern (49-1713) of BST. As thermal annealing time increases from 1.5 to 6 h, all the peak intensities are enhanced, indicating an increase of crystallinity. Figure 2b–e displays the cross-sectional FE-SEM images of 3D fabricated 50 and 60 wt% BST samples with different thermal annealing time. Hollow structures
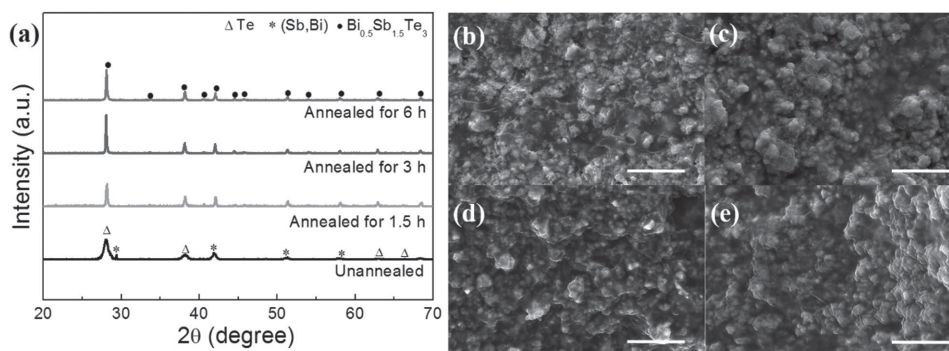


**Figure 2.** a) XRD patterns of 3D fabricated 60 wt% BST samples with various thermal annealing time at 350 °C. Cross-sectional FE-SEM images of 3D fabricated samples with different BST contents and various thermal annealing time at 350 °C: b) 50 wt%, 1.5 h; c) 60 wt%, 1.5 h; d) 60 wt%, 3 h; e) 60 wt%, 6 h. The scale bars are 10 μm.

**Table 1.** Structural parameters of 3D fabricated BST samples with different nominal compositions and thermal annealing conditions in comparison with the HPBST sample.

| Sample ID | Composition | Annealing process | | Density [g cm$^{-3}$] | Average grain size [nm] | BET surface area [m$^2$ g$^{-1}$] |
| --- | --- | --- | --- | --- | --- | --- |
| | | Temperature [°C] | Time [h] | | | |
| 3DBST50 | 50 wt% BST | 350 | 1.5 | 2.449 | 60.7 | 2.154 |
| 3DBST60 | 60 wt% BST | Unannealed | | 1.402 | 11.0 | |
| 3DBST60-1 | 60 wt% BST | 350 | 1.5 | 2.062 | 46.1 | 0.144 |
| 3DBST60-2 | 60 wt% BST | 350 | 3 | 2.467 | 62.2 | 1.918 |
| 3DBST60-3 | 60 wt% BST | 350 | 6 | 2.631 | 67.6 | 2.356 |
| HPBST | | | | 6.89[17] | | |

can be found in all samples, in which the formation of pores presumably results from the decomposition of photoresins during thermal annealing. This is in good agreement with the results found in energy-dispersive spectra (EDS) analysis (Figure S2, Supporting Information). It can been seen that carbons are gradually removed by prolonging thermal annealing time, as indicated by the decreasing carbon content from 17 to 10 wt% with increasing annealing time from 1.5 to 6 h (Table S1, Supporting Information), which implies the thermal decomposition of photoresins and therefore formation of amorphous carbons. Amorphous carbons were further inspected by Raman spectroscopy. As shown in Figure S3 (Supporting Information), the Raman-active modes of 3D fabricated 60 wt% BST sample are found around 1600 cm$^{-1}$ (G band, G means "graphitic") and 1360 cm$^{-1}$ (D band, D means "disordered"), which suggests the formation of amorphous carbons in the samples during thermal annealing process. The relative Raman intensity of the D and G bands is a measure of the degree of order in an amorphous carbon sample. These residual amorphous carbons are likely trapped inside the samples. The oxygen content notably decreases as thermal annealing time increases. However, a small quantity of oxygen can still be found in all samples, suggesting the incomplete decomposition of photoresins.

To reveal the generated pore structures, we measured the densities of 3D fabricated BST samples and the results are displayed in **Table 1**. The densities of 3D fabricated samples before and after thermal annealing are much smaller than that of hot-pressed $Bi_{0.5}Sb_{1.5}Te_3$ (HPBST) sample,[17] because of the existence of pores, amorphous carbon, and residual photoresins as indicated in Figure 1. The densities of 3D fabricated 60 wt% BST samples increase over thermal annealing time, presumably because of volume shrinkage of samples caused by decomposition of photoresins. The density of 50 wt% BST sample is found to be larger than that of 60 wt% BST sample probably because of its faster decomposition of photoresins. Based on the reduction of density, the porosities of 50 and 60 wt% BST samples can be estimated as ≈70% and 62%, respectively, if we assume that the photoresins are completely decomposed and all the carbons are removed. We then carried out the porosity measurements by using gas sorption surface area and pore size analyzer. The calculated Brunauer–Emmett–Teller (BET) results provide an estimation of surface areas of micro, meso, and macropores. As seen in Table 1, as thermal annealing time increases from 1.5, 3

to 6 h, the BET surface areas of 3D fabricated BST samples increase from 0.144, 1.918 to 2.356 m$^2$ g$^{-1}$, respectively, suggesting an increasing numbers of pores. These pores range from 1.8–20.4 nm in size distribution (Figure S4, Supporting Information). The average grain sizes of 3D fabricated BST samples were calculated from the XRD data by the Williamson–Hall method and summarized in Table 1. For the 3D fabricated 60 wt% sample, with the annealing time increasing from 1.5 to 6 h, the grain size increases from 46.1 to 67.6 nm, in accordance with the XRD results (Figure 2a) which show an increase of crystallinity with increasing annealing time.

Finally, we measured the TE properties of 3D fabricated samples. The energy conversion efficiency of a TE material is characterized by the dimensionless TE figure of merit ($ZT$), which is defined as $ZT = (S^2\sigma/\kappa_{total})T$, where $S$, $\sigma$, $\kappa_{total}$ are Seebeck coefficient, electrical conductivity, thermal conductivity, which consists of electronic thermal conductivity ($\kappa_{elec}$) and lattice thermal conductivity ($\kappa_{lattice}$), and $T$ is the absolute temperature, respectively.

**Figure 3** presents the TE characteristics of the 3D fabricated BST samples as a function of temperature in comparison with those of the HPBST sample reported by Poudel et al.[17] Figure 3a shows the measured $\kappa_{total}$ (dots) of four 3D fabricated BST samples. Extremely low values of $\kappa_{total}$ around 0.2 W m$^{-1}$ K$^{-1}$ at 44 °C were obtained in the 3DBST50 sample, which are much lower than that of HPBST sample,[17] respectively. This finding proves that the 3D fabrication is an effective way to decrease the thermal conductivity of TE materials. Moreover, $\kappa_{total}$ exhibits a nearly linear dependence on temperature for all the samples, which suggests that the sample is amorphous rather than crystalline. The reason is that thermal conductivity increases with temperature in amorphous materials which is opposite to that in crystalline materials.[29]

In order to better understand the amorphous characterics of 3D fabricated samples, we fitted the experimental results of thermal conductivity with theoretical models used in amorphous TE materials. In this regard, we used the Boltzmann transport equations (BTE) to calculate $\kappa_{elec}$ and used a model consists of multimechanisms to calculate $\kappa_{lattice}$. In the calculation of $\kappa_{elec}$, the contributions from both electrons ($e$) and holes ($h$) are combined by $\kappa_{elec} = (\kappa_e + \kappa_h) + T(S_e - S_h)^2 \sigma_e \sigma_h / (\sigma_e + \sigma_h)$. The expressions of the above transport properties are written as $\sigma_i = e^2 \langle \Sigma_i \rangle$, $S_i = \langle \Sigma_i (E_i - \mu) \rangle / [q_i T \langle \Sigma_i \rangle]$, and
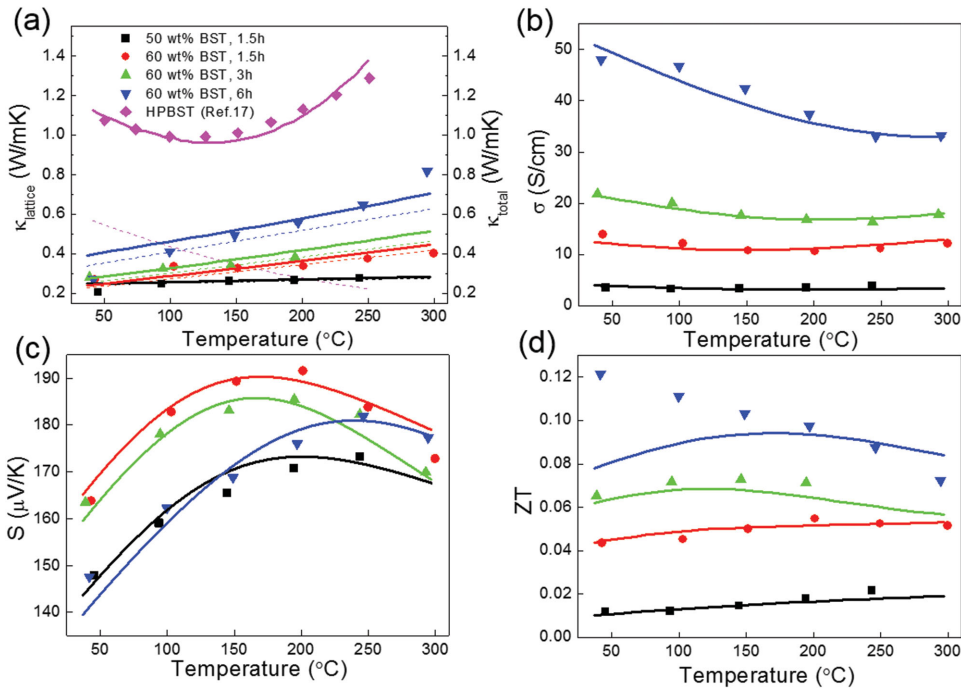
**Figure 3.** Temperature dependence of TE properties of the 3D fabricated BST samples. a) Lattice thermal conductivity ($\kappa_{lattice}$) and total thermal conductivity ($\kappa_{total}$) in comparison with that of hot-pressed sample,[17] where the dashed and solid lines correspond to the calculated $\kappa_{lattice}$ and $\kappa_{total}$, respectively, b) electrical conductivity ($\sigma$), c) Seebeck coefficient ($S$) and d) $ZT$. The dots with error bar are experimental data and the curves with the same colors are the corresponding theoretical calculation results. Symbol representations: ■ 50 wt% BST, annealed for 1.5 h; ● 60 wt% BST, annealed for 1.5 h; ▲ 60 wt% BST, annealed for 3 h; ▼ 60 wt% BST, annealed for 6 h; ◆ HPBST. All these samples were thermally annealed at 350 °C.

$\kappa_i = [\langle \Sigma_i (E_i - \mu)^2 \rangle - \langle \Sigma_i (E_i - \mu) \rangle^2 / \langle \Sigma_i \rangle] / T$,[26,27] where $i = e, h$ and

$$\langle \Sigma_i (E - \mu)^n \rangle = \int dE_i \Sigma_i (E_i - \mu)^n \left( -\frac{\partial f_i}{\partial E_i} \right) \quad (1)$$

Here $n = 0, 1, 2$. $q_e = -|e|$ and $q_h = |e|$ are the charge of electrons and holes, respectively. $E_e$ and $E_h$ are the energies, $\mu$ is the chemical potential, $f_e$ and $f_h$ are the Fermi–Dirac distribution functions, $\Sigma_e$ and $\Sigma_h$ are the transport distribution functions.[28] Scattering mechanisms such as carrier-impurity scattering, carrier-phonon scattering, and carrier-boundary scattering are considered. The parameters used are presented in Table S2 (Supporting Information). In the calculation of $\kappa_{lattice}$, we employed a model for amorphous materials which takes into account the phonon scatterings by pores.[29–31] This model starts from $\kappa_{lattice} = C_V v_p l / 3$ where $C_V$ is the specific heat which can be estimated by Debye model,[32] $v_p$ is the phogroup velocity, and $l$ is the phonon mean free path (MFP).[29] The phonon frequency-dependent MFP is calculated by $l^{-1} = A v^{1.2}$ when $v < v_\xi$ and $l^{-1} = B v^4$ when $v < v_\Xi$, where $v_\xi$ and $v_\Xi$ are transition frequencies of different scattering regimes.[30] $A$ and $B$ are fitting parameters which can be found in Table S3 (Supporting Information). The former MFP, which is valid for low frequency, considers the phonon scattering by two-level states, while the latter MFP, which is valid for intermediate frequency, considers the phonon scattering by pores.[30] For higher frequency scattering regime, $v_\Xi < v < v_D$, the hopping mechanism dominates where the

hopping relaxation time $\tau_{hop}^{-1} \propto T$. Its contribution to $\kappa_{lattice}$ is calculated by[28] $C_V l_0^2 / 3 \tau_{hop} = C_V C T / 3$, where $l_0$ is the hopping distance, $v_D$ is the Debye frequency and $C$ is fitting parameter as shown in Table S3 (Supporting Information). At room temperature, the high-frequency scattering is most important which causes a linear dependence of $\kappa_{lattice}$.[31] The calculated $\kappa_{lattice}$ (dotted curves) and $\kappa_{elec} + \kappa_{lattice}$ (solid curves) are shown in Figure 3a. Our theoretical results are in good agreement with the measured values. We find that the calculated $\kappa_{elec}$ is much less than the calculated $\kappa_{lattice}$ since the carrier concentration of BST samples is small. The $\kappa_{lattice}$ in the HPBST sample reported by Poudel et al.[17] (purple dashed curve) is also plotted for comparison. Our theoretical calculations confirm that the temperature dependence of $\kappa_{lattice}$ in 3D fabricated samples is opposite to that in HPBST sample. This finding implies that our 3D printing fabrication method is a promising way to fabricate "phonon-glass" TE materials.

Figure 3b shows the measured temperature dependence of electrical conductivity together with the theoretical calculated values using Equation (1) and $\sigma = \sigma_e + \sigma_h$.[27] The calculated results fit the experimental data very well with reasonable parameters as shown in Table S3 (Supporting Information). We find that higher BST contents lead to higher $\sigma$ values. As the annealing time increases from 1.5 to 6 h, the $\sigma$ value of 3DBST60 sample is increased by 246%, presumably due to increased carrier concentration. The highest $\sigma$ value of ≈50 S cm$^{-1}$ was obtained in the 3DBST60 sample at 43 °C, which is one order of magnitude lower than

that of hot-pressed samples. The reason is that the carrier concentration is significantly low in our 3D fabricated amorphous samples. Future work will aim at introducing additional dopants to increase the electrical conductivity in such 3D fabricated samples.

Figure 3c shows the measured temperature dependence of $S$ for the 3D fabricated BST samples together with the theoretical calculated values using Equation (1) and $S = (S_e \sigma_e + S_h \sigma_h)/(\sigma_e + \sigma_h)$.[27] Positive $S$ indicates that the samples are p-type in which holes dominate the charge transport. Clearly, the sample which has more BST content exhibits higher $S$ value. The highest $S$ value of 191 μV K$^{-1}$ at 151 °C is found in the 3DBST60 sample with an annealing time of 1.5 h.

The $ZT$ values of the 3D fabricated BST samples were obtained from the above experimental and theoretical results, as shown in Figure 3d. All 3DBST60 samples exhibit much higher $ZT$ values than 3DBST50 sample because of their higher values of $\sigma$ and $S$. Besides, for the 60 wt% BST samples, the $ZT$ values increase as the annealing time increases because of the $\sigma$ enhancement as shown in Figure 3b. Thus, increasing the annealing time has demonstrated an effective means to increase $ZT$ values of 3D fabricated BST samples. The best $ZT$ value is 0.12 at 43 °C for the 3DBST60 sample with an annealing time of 6 h.

In conclusion, we have demonstrated a promising 3D printing technique, as an alternative to hot-pressing and spark plasma sintering methods, to fabricate thermoelectric materials. Interestingly, amorphous behavior of thermal conductivity was found in these 3D fabricated samples, as observed by a linear increase of lattice thermal conductivity, which is a typical "phonon-glass" phenomenon and confirmed by theoretical calculations. An ultralow thermal conductivity of 0.2 W m$^{-1}$ K$^{-1}$ was therefore obtained. Yet the resulting $ZT$ value is low due to poor electrical conductivity of as-fabricated BST samples, which can be improved by additional doping. It can be envisioned that 3D printing technique enables the generation of flexible, any shaped thermoelectric materials, which are otherwise difficult to obtain by traditional methods, thereby largely extending thermoelectric applications.

## Experimental Section

*Chemicals and Materials*: All the reagents used in the experiments were used without further purification, including an epoxy resin (3,4-epoxycyclohexylmethyl-3,4-epoxycyclohexane carboxylate, Jingzhou Xinjing Chemical Co., Ltd), a diluent (3-ethyl-3-oxetanemethanol, Nantong Synasia Co., Ltd), a cationic photoinitiator (triarylsulfonium hexafluoroantimonate salts, Nantong Synasia Co., Ltd), a photosensitizer (PSS-303, Nantong Synasia Co., Ltd), and Formlabs Clear Photoresins (Formlabs Inc.).

*BST Powder Preparation*: High-purity (over 99.999%) Bi, Sb, and Te granules were weighed with a nominal composition of $Bi_{0.5}Sb_{1.5}Te_3$. Then the weighed materials were loaded with stainless steel balls into stainless steel vials and sealed inside a glove box. The planetary mill operating at 500 rpm was used for mechanical alloying. Wet milling used hexane as the grinding media. The synthesized powders were obtained by ball milling for 100 h followed by drying overnight inside a nitrogen glove box.

*Photoresin Formulations*: The composite resins were formulated by stirring a mixture of all components at ambient temperature in light-sealed 250 mL flasks until homogenous solutions were obtained. A typical procedure of preparing composite resins for 3D printing/fabrication is described as follows. A mixture of triarylsulfonium hexafluoroantimonate salts (9 g) and PSS-303 (0.9 g) was dissolved in a mixed solution of 3,4-epoxycyclohexylmethyl-3,4-epoxycyclohexane carboxylate (69 g) and 3-ethyl-3-oxetanemethanol (39 g) under stirring at room temperature. Then BST powders were fully dispersed in the above mixture solution with a solid content of 40, 50, and 60 wt%, respectively. The composite resins for 3D printing were made of Formlabs Clear Photoresins and BST powders at contents of 1, 3, and 5 wt%, respectively.

*SLA Apparatus*: SLA processes were performed on a Form 1+ SLA 3D printer (Formlabs Inc.) equipped with a 405 nm-laser. And a layer thickness of 100 μm was chosen for the printing process. By utilizing the 3D printing principle, for 3D fabricating process, the composite resins were cured by optical equipment with 405 nm-laser diode (Nichia Corporation) at power of 1.2 W to generate the BST bulk samples. The photocuring time was adjusted to obtain a curing depth of about 20 μm for the resins. The obtained samples were cleaned with IPA several times, and then dried at 90 °C overnight in a vacuum oven.

*Thermal Annealing Process*: All the BST samples were thermally annealed at atmospheric pressure in a tubular furnace (BTF-1200C, Anhui BEQ Equipment Technology Co., Ltd) at 350 °C under a constant flow of Ar gas.

*Characterizations and Measurements*: The electrical transport properties involving $\sigma$ and $S$ were measured from 42 to 300 °C using a thermoelectric measurement system (LSR-3/1100; Linseis, Germany) in a helium atmosphere. The thermal diffusivity ($D$) was measured using a laser flash apparatus (LFA 1000; Linseis, Germany) and the specific heat ($C_p$) measurements which were performed on a DSC Q2000 TA differential scanning calorimeter. The density, $d$, was measured by Archimedes' method and finally, the thermal conductivity was calculated using the equation $\kappa = D \times C_p \times d$. X-ray diffraction pattern data were collected with a Bruker AX D8 Advance diffractometer with nickel filtered Cu K$\alpha$ radiation ($\lambda$ = 1.5406 Å). FE-SEM (Hitachi S-520) was used to study the microstructure of the samples. Sample porosities were evaluated by a Quadrasorb evo gas sorption surface area and pore size analyzer (Quantachrome Instruments, USA) and the BET method was used to calculate the specific surface areas. Raman spectra were obtained on an XploRA PLUS Raman microscope (Horiba JY, France) under a laser excitation at 638 nm. Spectra was acquired over a range of 300–2200 cm$^{-1}$ with sufficient averaging to allow for reliable fitting.

[1] C. W. Hull(UVP, Inc.), *U.S. 4575330*, **1986**.
[2] M. He, K. Song, H. Mo, J. Li, D. Pan, Z. Liang, *J. Funct. Polym.* **2015**, *28*, 102.
[3] J. H. Sandoval, K. F. Soto, L. E. Murr, R. B. Wicker, *J. Mater. Sci.* **2007**, *42*, 156.
[4] S. Kumar, M. Hofmann, B. Steinmann, E. J. Foster, C. Weder, *ACS Appl. Mater. Interfaces* **2012**, *4*, 5399.
[5] D. Karalekas, K. Antoniou, *J. Mater. Process Technol.* **2004**, *153–154*, 526.
[6] M. Gurr, D. Hofmann, M. Ehm, Y. Thomann, R. Kübler, R. Mülhaupt, *Adv. Funct. Mater.* **2008**, *18*, 2390.
[7] J. R. Tumbleston, D. Shirvanyants, N. Ermoshkin, R. Janusziewicz, A. R. Johnson, D. Kelly, K. Chen, R. Pinschmidt, J. P. Rolland, A. Ermoshkin, E. T. Samulski, J. M. DeSimone, *Science* **2015**, *347*, 1349.
[8] M. S. Mannoor, Z. Jiang, T. James, Y. L. Kong, K. A. Malatesta, W. O. Soboyejo, N. Verma, D. H. Gracias, M. C. McAlpine, *Nano Lett.* **2013**, *13*, 2634.
[9] M. D. Symes, P. J. Kitson, J. Yan, C. J. Richmond, G. J. T. Cooper, R. W. Bowman, T. Vilbrandt, L. Cronin, *Nat. Chem.* **2012**, *4*, 349.
[10] P. J. Kitson, M. D. Symes, V. Dragone, L. Cronin, *Chem. Sci.* **2013**, *4*, 3099.
[11] G. Chisholm, P. J. Kitson, N. D. Kirkaldy, L. G. Bloor, L. Cronin, *Energy Environ. Sci.* **2014**, *7*, 3026.
[12] K. Sun, T.-S. Wei, B. Y. Ahn, J. Y. Seo, S. J. Dillon, J. A. Lewis, *Adv. Mater.* **2013**, *25*, 4539.
[13] J. Wang, M. Yang, Y. Zhu, L. Wang, A. P. Tomsia, C. Mao, *Adv. Mater.* **2014**, *26*, 4961.
[14] S.-Z. Guo, F. Gosselin, N. Guerin, A.-M. Lanouette, M.-C. Heuzey, D. Therriault, *Small* **2013**, *9*, 4118.
[15] D. B. Kolesky, R. L. Truby, A. S. Gladman, T. A. Busbee, K. A. Homan, J. A. Lewis, *Adv. Mater.* **2014**, *26*, 3124.
[16] B. G. Compton, J. A. Lewis, *Adv. Mater.* **2014**, *26*, 5930.
[17] B. Poudel, Q. Hao, Y. Ma, Y. Lan, A. Minnich, B. Yu, Z. Yan, D. Wang, A. Muto, D. Vashaee, Z. Chen, J. Liu, M. S. Dresselhaus, G. Chen, Z. Ren, *Science* **2008**, *320*, 634.
[18] Y. Ma, Q. Hao, B. Poudel, Y. C. Lan, B. Yu, D. Z. Wang, G. Chen, Z. F. Ren, *Nano Lett.* **2008**, *8*, 2580.
[19] W. J. Xie, J. He, H. J. Kang, X.F. Tang, S. Zhu, M. Laver, S. Y. Wang, J. R. D. Copley, C. M. Brown, Q. J. Zhang, T. M. Tritt, *Nano Lett.* **2010**, *10*, 3283.
[20] T. Takabatake, K. Suekuni, T. Nakayama, E. Kaneshita, *Rev. Mod. Phys.* **2014**, *86*, 669.
[21] C. Xiao, J. Xu, B. Cao, K. Li, M. Kong, Y. Xie, *J. Am. Chem. Soc.* **2012**, *134*, 7971.
[22] L. Wu, Q. Meng, C. Jooss, J.-C. Zheng, H. Inada, D. Su, Q. Li, Y. Zhu, *Adv. Funct. Mater.* **2013**, *23*, 5728.
[23] S. Bhattacharya, A. Bohra, R. Basu, R. Bhatt, S. Ahmad, K. N. Meshram, A. K. Debnath, A. Singh, S. K. Sarkar, M. Navneethan, Y. Hayakawa, D. K. Aswal, S. K. Gupta, *J. Mater. Chem. A* **2014**, *2*, 17122.
[24] J. S. Tse, K. Uehara, R. Rousseau, A. Ker, C. I. Ratcliffe, *Phys. Rev. Lett.* **2000**, *85*, 114.
[25] Y. Nakamura, M. Isogawa, T. Ueda, S. Yamasaka, H. Matsui, J. Kikkawa, S. Ikeuchi, T. Oyake, J. Shiomi, A. Sakai, *Nano Energy* **2015**, *12*, 845.
[26] J. Zhou, R. G. Yang, *Phys. Rev. B* **2010**, *82*, 075324.
[27] J. Zhou, X. B. Li, G. Chen, R. G. Yang, *Phys. Rev. B* **2010**, *82*, 115308.
[28] G. D. Mahan, J. O. Sofo, *Proc. Natl. Acad. Sci. USA* **1996**, *93*, 7436.
[29] D. G. Cahill, R. O. Pohl, *Solid State Commun.* **1989**, *70*, 927.
[30] J. M. Grace, A. C. Anderson, *Phys. Rev. B.* **1986**, *33*, 7186.
[31] A. Jagannathan, R. Orbach, O. Entin-Wohlman, *Phys. Rev. B* **1989**, *39*, 13465.
[32] W. K. Hildebrand, *M.Sc. Thesis*, University of Manitoba (Winnipeg), **2009**.